Frequency-encoded linear cluster states with coherent Raman photons

Dale Scerri,* Ralph N. E. Malein, Brian D. Gerardot, and Erik M. Gauger†
SUPA, Institute of Photonics and Quantum Sciences, Heriot-Watt University, EH14 4AS, United Kingdom

(Received 17 February 2018; published 14 August 2018)

Entangled multiqubit states are an essential resource for quantum information and computation. Solid-state emitters can mediate interactions between subsequently emitted photons via their spin, thus offering a route towards generating entangled multiphoton states. However, existing schemes typically rely on the excitation-relaxation of the emitter, resulting in single photons limited by the emitter's radiative lifetime, suffering from considerable practical limitations, for self-assembled quantum dots most notably the limited spin coherence time due to Overhauser magnetic field fluctuations. We here propose an alternative approach based on a spin-Λ system that overcomes the limitations of previous proposals. Studying the example of spin-flip Raman scattering of self-assembled quantum dots in Voigt geometry, we argue that weakly driven hole spins constitute a promising platform for the practical generation of frequency-entangled photonic cluster states.

DOI: 10.1103/PhysRevA.98.022318

I. INTRODUCTION

Robust highly entangled "cluster" states are of paramount importance for measurement-based quantum computation [1–4]. The experimental challenges of obtaining high-dimensional cluster states can be significantly reduced by probabilistically "fusing" qubits from adjacent one-dimensional (1D) linear cluster (LC) states [5–7], or "gluing" together microclusters [8]. Several platforms for generating photonic LC states have been proposed, varying from condensed matter emitters such as quantum dots [6,9–13] and crystal defects [11,14] to parametric down-conversion [15,16], all presenting their own sets of advantages and challenges. Solid-state-based protocols typically make use of pulsed excitations to drive optical transitions in a matter qubit to entangle the emitter's spin degree of freedom with the polarization of subsequently emitted photons. Encouragingly, a photonic LC of length two (LC_2) has recently been demonstrated experimentally, showing that the entanglement in this setup could persist for up to five consecutively emitted photons [13].

While conceptually elegant and ostensibly deterministic, real-world imperfections pose significant barriers to the experimental realization of protocols such as the ones introduced by Refs. [9,10,17,18]. For the III-V platform, these include phonon dephasing of excited states [19], modified selection rules as a consequence of hole mixing as well as a transverse (Voigt) component of the Overhauser field [20–23], and limited spin lifetimes due to Overhauser field fluctuations [20,24–27]. Decoupling techniques [28–34] and control of the nuclear environment [27,35–37] overcome the latter but provide no remedy for other error sources. Shortcomings of real quantum dots thus put a limit to the size of cluster state achievable and render genuinely deterministic operation impractical for the current experimental state of the art.

In contrast to direct pulsed excitation, we here propose employing a weak (subsaturation) continuous wave (cw) laser to drive the Zeeman-detuned transitions of a hole spin for entangling the spin with the frequency of Raman scattered photon [38]. We show such a setup overcomes the experimental barriers suffered by previous schemes, which rely on excitation and relaxation of the emitter: in particular, our protocol is impervious to phonon dephasing, robust against fluctuations of the Overhauser field, and unaffected by heavy-hole (hh) light-hole (lh) mixing. This comes at the cost making the protocol probabilistic, however, we show that LC states of sufficient length to serve as building blocks for fusion [5] can be produced at high rates and fidelity based on current experimental capabilities. Furthermore, extended versions of our protocol mitigating its probabilistic limitations (while keeping its robustness) are possible (see Appendix H). Our work thus shows that the significant divide between elegant theoretical proposals and experimental progress in the generation of linear cluster states can be overcome. The approach we present has scope for extension to other quantum photonic platforms sharing a similar Λ structure, including defects in wide-band-gap semiconductors [39,40] and superconducting artificial atoms [41–43]. Mathematical detail and extensions of the main protocol can be found in Appendix D.

II. MODEL

Despite its many attractive features for quantum metrology and quantum information [24,44], the spin of an electron trapped in an epitaxial quantum dot suffers from rapid ensemble dephasing due to the hyperfine interaction with $\sim 10^4$–10^6 randomly fluctuating nuclear spins of the host material. This typically results in a loss of coherence on the order of nanoseconds [23–26]. By contrast, the p-orbital-like wave function of hole-spin states vanishes at the location of the nuclear spins, which suppresses the Fermi-contact interaction, leaving only the much weaker dipole-dipole interaction as the main source of dephasing [21,45–47]. Strain lifts the degeneracy of

*ds32@hw.ac.uk
†e.gauger@hw.ac.uk

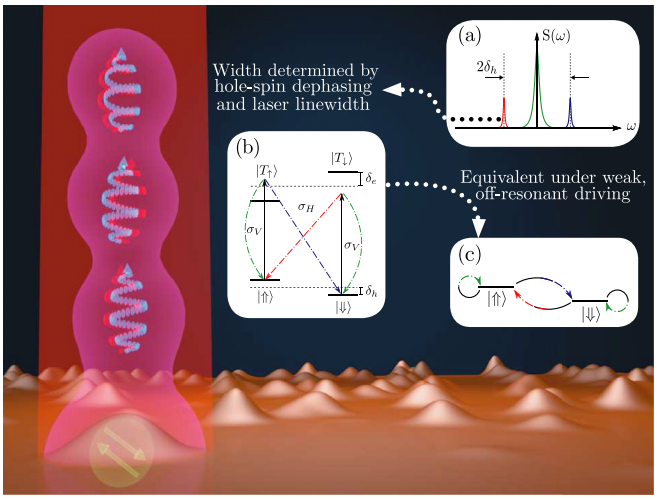

FIG. 1. Background: artistic depiction of our protocol. Inset (a): schematic of the emission spectrum showing the presence of the Raman sidebands. Inset (b): schematic illustration of the scattering processes involving the two ground hole-spin states. The black arrows denote the laser driving on resonance with the unperturbed transitions (dashed lines), whereas the green, red, and blue arrows denote the Rayleigh, red-detuned, and blue-detuned events, respectively. Inset (c): simple schematic of the scattering processes involved in the weak, detuned driving limit.

the $J = \frac{3}{2}$ hole states, resulting in energetically split heavy ($J_z = \pm\frac{3}{2}$) and light ($J_z = \pm\frac{1}{2}$) holes, the former being closer to the valence band edge (see Fig. 1). Rashba or Dresselhaus spin-orbit coupling may may play a role in limiting factor for the application of these hole spins in quantum information, which were shown, both theoretically [48] and experimentally [49], to limit the spin relaxation rate. However, we note that this spin-orbit coupling is still more detrimental to electron than hole spins [48].

However, chiefly due to strain anisotropy in the QD, a finite admixture of these states is always present (the effects on hole-based multiphoton entanglement schemes are briefly discussed in Appendix F 2). In the following, we denote the (Zeeman) spin state of the heavy hole as $|\Uparrow\rangle$ and $|\Downarrow\rangle$ whereas the electron spin states are $|\uparrow\rangle$ and $|\downarrow\rangle$. In this notation, the positively charged X^{1+} transition $|\Uparrow\rangle \leftrightarrow |T_\uparrow\rangle = |\Uparrow\Downarrow, \uparrow\rangle$ couples to σ^--polarized light and $|\Downarrow\rangle \leftrightarrow |T_\downarrow\rangle = |\Uparrow\Downarrow, \downarrow\rangle$ to σ^+ light. In the presence of an external magnetic field in Voigt geometry, the otherwise dipole-forbidden diagonal Raman transitions are unlocked (see Fig. 1) [50]. For weakly off-resonantly driven hole spins, the width of these Raman transitions is solely limited by the laser linewidth and ground-state spin dephasing [51,52], making them attractive candidates for single-photon sources, as well as being attractive spin-spin qubit entanglers due to the spin's rich level scheme and selection rules [53,54].

Wishing to exploit such Raman photons for LC generation we consider a self-assembled quantum dot in the Voigt geometry, with the applied magnetic field B strong enough to dominate over nuclear Overhauser field fluctuations (see Appendix B). The applied B field (without loss of generality along the x axis) then defines the basis of spin eigenstates. We also include a cw laser field that is resonant with the unperturbed transition of the QD [Fig. 1(a)]. In a frame rotating with the laser frequency (after performing the RWA), the QD Hamiltonian in the Zeeman basis reads as

$$\begin{aligned} H =& \delta_h(|\Uparrow\rangle\langle\Uparrow| - |\Downarrow\rangle\langle\Downarrow|) + \delta_e(|T_\downarrow\rangle\langle T_\downarrow| - |T_\uparrow\rangle\langle T_\uparrow|) \\ &- \left(\frac{\Omega_H}{2}|T_\uparrow\rangle\langle\Downarrow| + \frac{\Omega_H}{2}|T_\downarrow\rangle\langle\Uparrow| + \frac{\Omega_V}{2}|T_\downarrow\rangle\langle\Downarrow| \right. \\ &\left. + \frac{\Omega_V}{2}|T_\uparrow\rangle\langle\Uparrow| + \text{H.c.}\right), \end{aligned} \tag{1}$$

where $\delta_{e,h}$ are the electron and hole Zeeman splittings, respectively, $\Omega_{H/V}$ are the Rabi frequencies for the horizontally and vertically polarized transitions, and H.c. denotes the Hermitian conjugate. We simulate the scattering events via Monte Carlo trajectories with jump operators for all allowed transitions, occurring with equal rates γ. This results in an effective (non-Hermitian) Hamiltonian $H_{\text{eff}} = H - \frac{i\hbar}{2}\gamma\sum_n C_n^\dagger C_n$, where the sum goes over the collapse operators [55,56]. This nonunitary evolution of the system generates photons outside of the QD's Hilbert space, which build the LC states we are interested in. More specifically, each "experiment" is simulated as a quantum jump simulation, where an LC_n state is successfully measured if the correct n scattering events occur within the designated time bins. The success rate is then calculated by averaging over the results.

III. PROTOCOL

Figure 1(b) shows that the emission of blue- and red-detuned Raman spin-flip photons from a single quantum dot must alternate, provided that the scattering rate is faster than the hole spin-flip time. We build on this correlation between spin and photon color to develop a protocol for generating an entangled LC state (filtering out Rayleigh scattered photons via their orthogonal polarization). As an intrinsic drawback of Raman spin flips, the time at which a photon is scattered is not known prior to its detection. In the following, we assume that there is exactly one Raman scattering event per time bin T_B (albeit at a random time within the bin, see Fig. 2). The overall probability and ways of circumventing this limitation [57] will be discussed later. Figure 3 contains a diagrammatic representation of a successful run of our protocol. Let us trace the evolution of the joint spin-photon state step by step: we start with the hole spin initialized in the superposition state $|\Uparrow\rangle + |\Downarrow\rangle$ (ignoring normalization factors) and precessing at its Larmor frequency. Let the accumulated phase prior to the first scattering event be $\phi_1 = \delta_h\tau_1$ [denoted by the matrix $U_p(\phi_1)$ in Fig. 3], then a Raman spin flip (T_s in Fig. 3) evolves the state to

$$e^{-i\frac{\phi_1}{2}}|\Uparrow\rangle + e^{i\frac{\phi_1}{2}}|\Downarrow\rangle \rightarrow e^{-i\frac{\phi_1}{2}}|\Downarrow B_1\rangle + e^{i\frac{\phi_1}{2}}|\Uparrow R_1\rangle, \tag{2}$$

where the labels B_1 (R_1) inside the ket denote the first emitted blue (red) photon. A subsequent period of free precession $\tau_2 = T_B - \tau_1$ until the end of the time bin T_B results in a phase $\phi_2 = \delta_h\tau_2$. We now apply a $\pi/2$ Y rotation ($U_r = Y_{\frac{\pi}{2}}$ in Fig. 3), yielding the state

$$e^{-i\frac{\phi_1}{2}}|\Uparrow B_1\rangle + e^{-i\frac{\phi_1}{2}}|\Downarrow B_1\rangle + e^{i\frac{\phi_1}{2}}|\Uparrow R_1\rangle - e^{i\frac{\phi_1}{2}}|\Downarrow R_1\rangle, \tag{3}$$

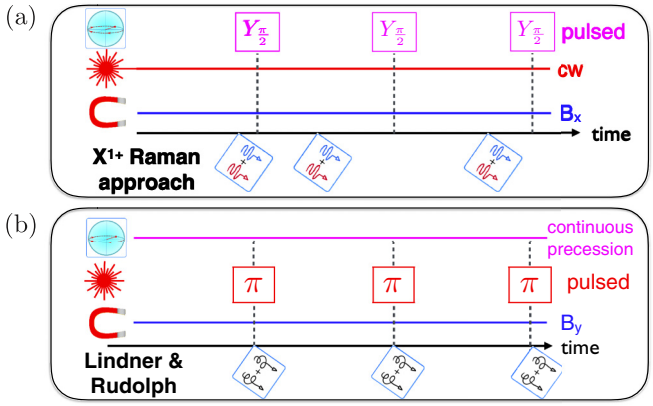

FIG. 2. (a) Schematic representation of our protocol. The spin precesses in a constant magnetic field in Voigt geometry. Driven weakly and off resonantly, the hole spin scatters Raman-detuned photons at random intervals. The timing between Y pulses T_B should be chosen so as to maximize the probability of getting a single scattering event between the pulses. (b) Schematic of the original Lindner and Rudolph proposal for comparison. Instead of a gated Y rotation, an external field in Voigt geometry causes the spin to precess continuously, with optical π pulses applied at the appropriate times to excite the emitter.

where $\chi_1 := \phi_1 - \phi_2$. The next Raman scattering event will have been preceded by another spin precession angle ϕ_3 resulting in

$$e^{-i\frac{\phi_3}{2}}e^{-i\frac{\chi_1}{2}}|\Downarrow B_1 B_2\rangle + e^{i\frac{\phi_3}{2}}e^{-i\frac{\chi_1}{2}}|\Uparrow B_1 R_2\rangle + e^{-i\frac{\phi_3}{2}}e^{i\frac{\chi_1}{2}}|\Downarrow R_1 B_2\rangle - e^{i\frac{\phi_3}{2}}e^{i\frac{\chi_1}{2}}|\Uparrow R_1 R_2\rangle. \quad (4)$$

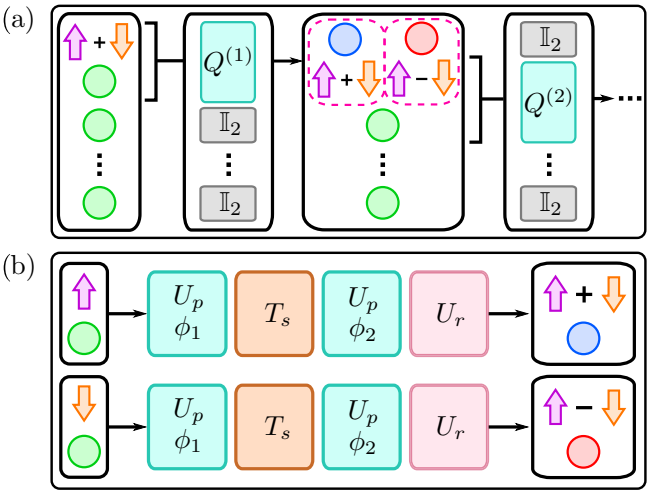

FIG. 3. (a) Diagrammatic representation of the spin-photon entangling process for the first emitted photon. The initial spin state ($|\Uparrow\rangle + |\Downarrow\rangle$) and first laser photon to be scattered (upmost green circle) undergo a joint transformation $Q^{(1)}$, resulting either in a red- or a blue-detuned Raman photon that is entangled with the hole spin. $Q^{(2)}$ includes the second Raman process and entangles the newly scattered with the previous photon. (b) Breakdown of the $Q^{(i)}$ operation through its action on spin basis states: the sequence of operations transforms includes two periods of free spin precession U_p, the Raman scattering process T_S, and a $\pi/2$ Y rotation U_r. A full matrix representation of $Q^{(i)}$ is given in Appendix C.

The spin precesses further by ϕ_4 before we apply the next $Y_{\frac{\pi}{2}}$ rotation, yielding

$$\begin{aligned} &e^{-i\frac{\phi_3}{2}}e^{i\frac{\phi_4}{2}}e^{-i\frac{\chi_1}{2}}|\Downarrow B_1 B_2\rangle + e^{i\frac{\phi_3}{2}}e^{-i\frac{\phi_4}{2}}e^{-i\frac{\chi_1}{2}}|\Uparrow B_1 R_2\rangle \\ &\quad + e^{-i\frac{\phi_3}{2}}e^{i\frac{\phi_4}{2}}e^{i\frac{\chi_1}{2}}|\Downarrow R_1 B_2\rangle - e^{i\frac{\phi_3}{2}}e^{-i\frac{\phi_4}{2}}e^{i\frac{\chi_1}{2}}|\Uparrow R_1 R_2\rangle \\ &:= e^{-i\frac{\chi_2}{2}}e^{-i\frac{\chi_1}{2}}|\Downarrow B_1 B_2\rangle + e^{i\frac{\chi_2}{2}}e^{-i\frac{\chi_1}{2}}|\Uparrow B_1 R_2\rangle \\ &\quad + e^{-i\frac{\chi_2}{2}}e^{i\frac{\chi_1}{2}}|\Downarrow R_1 B_2\rangle - e^{i\frac{\chi_2}{2}}e^{i\frac{\chi_1}{2}}|\Uparrow R_1 R_2\rangle. \end{aligned} \quad (5)$$

Let us stop at this point and, for clarity, consider the resulting state without its free precession phases

$$|\Downarrow B_1 B_2\rangle + |\Uparrow B_1 R_2\rangle + |\Downarrow R_1 B_2\rangle - |\Uparrow R_1 R_2\rangle. \quad (6)$$

Using the photon qubit encoding $|B_i\rangle = |1_i\rangle$, $|R_i\rangle = |0_i\rangle$, the state following the final $Y_{\frac{\pi}{2}}$ rotation is given by

$$\begin{aligned} &|\Uparrow 1_1 1_2\rangle + |\Downarrow 1_1 1_2\rangle + |\Uparrow 1_1 0_2\rangle - |\Downarrow 1_1 0_2\rangle \\ &\quad + |\Uparrow 0_1 1_2\rangle + |\Downarrow 0_1 1_2\rangle - |\Uparrow 0_1 0_2\rangle + |\Downarrow 0_1 0_2\rangle. \end{aligned} \quad (7)$$

In Appendix D, we show that, whether the spin is measured to be in the $|\Uparrow\rangle$ or $|\Downarrow\rangle$ state, the resulting photonic state ($S_+^{(2)}$ or $S_-^{(2)}$, respectively) indeed corresponds to LC_2. Further, we show that the above protocol generalizes trivially to the production of LC states of arbitrary length. Crucially, reintroducing the above precession phases keeps the state local unitarily (LU) equivalent to LC_2. The phases become known post measurement through the time stamps of the detection clicks, and in Appendix I, we discuss how to make allowances for them for a tomographic reconstruction of the LC state. [58]

IV. RESULTS

We now analyze the quality and success probability of our protocol. We begin with the rate for Raman scattering events followed by the success probability of a string of n Raman photons with one per time bin. Figure 4(a) shows the Raman scattering rate and its dependence on both B and Ω_V. Comparison with numerical simulations shows that this rate is well approximated by the transition probability obtained by treating the weak driving field perturbatively to second order (see Appendix A):

$$\gamma_{\text{pert}} = \frac{1}{8}\frac{\Omega_V^2 \gamma}{\Delta^2}, \quad (8)$$

provided $B \gtrsim 100$ mT and subsaturation $\Omega_V \lesssim \gamma/\sqrt{2}$ (with γ being the spontaneous emission rate), where $\Delta = \delta_e + \delta_h$. We proceed to determine the optimal duration T_B (i.e., the free precession time between Y rotations) for maximizing the probability of obtaining a single Raman event per time bin. Adopting $B = 100$ mT and $\Omega_V = 0.2\gamma/\sqrt{2}$ (taking $\gamma = 1\ \text{ns}^{-1}$), we calculate the number of successful trials with one Raman photon per T_B interval (time interval between U_r rotations in Fig. 3) in n successive time bins. Figure 4(c) illustrates the results of Monte Carlo simulations using the QUTIP package [55,56] for $n = 1$ to 4 scattering events, suggesting that $T_B \approx 0.5\ \mu$s is close to optimal. We have the relation $P_s(n) = P_s(1)^n$ between the success probability for a single bin and that of n bins.

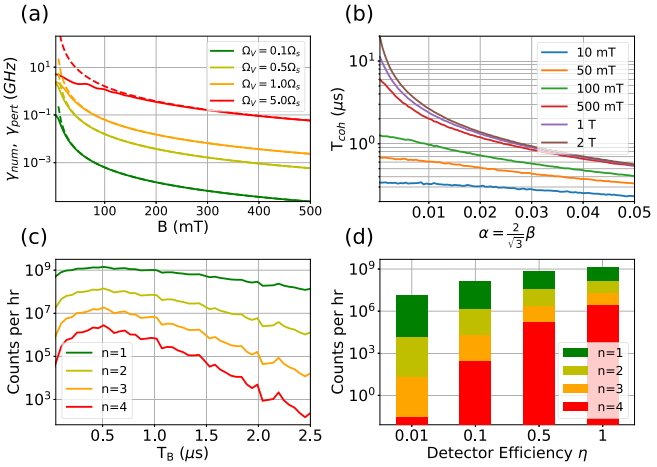

FIG. 4. (a) Perturbative calculation γ_{pert} (dashed line) and numerical value γ_{num} (solid line) of the Raman scattering rate as a function of B for various driving strengths (from bottom to top: $\Omega_V = 0.1, 0.5, 1,$ and $5\,\Omega_s$). (b) Coherence time for the pseudospin initially prepared perpendicular to the applied external magnetic field with mixing factor $\alpha = \frac{2}{\sqrt{3}}\beta$ for various external field strengths. The Overhauser field was taken to have a spread of 14 mT (from bottom to top: $B = 0.01, 0.05, 0.1, 0.5, 1,$ and 2 T). (c) Number of successful n-photon correlations per hour against T_B, with $\eta = 1$ for the ideal scenario $B = 100$ mT, $\Omega = 0.2\gamma/\sqrt{2}$, and $g_h^x = 0.1$ (from top to bottom: $n = 1,\ 2,\ 3,$ and 4). (d) Success probabilities optimized for $T_B = 500$ ns [by minimizing Eq. (9)] against η, decreasing with increasing n.

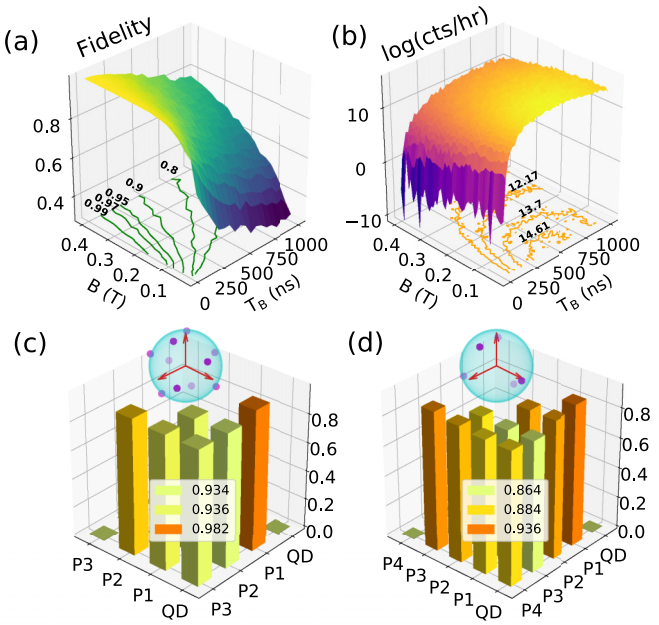

FIG. 5. (a) Fidelity of the LC_4 state in the presence of the Overhauser field against applied field magnitude and single time-bin duration for a mixed hh-lh spin state. Overhauser fluctuations were 14 mT [23], with $g_h^x = 0.1$, $\alpha = 0.01$, and a completely unpolarized spin bath. (b) Natural logarithm of the success counts for a string of four photons. The overall detector efficiency was taken to be $\eta = 1$. The count rate increases with T_B until probability of multiple events in a single bin becomes significant. An increasing B field decreases the count rate as predicted from Eq. (8). (c), (d) Normalized LE for between pairwise combinations of a spin and three (c) or four (d) scattered photons, respectively. Due to computational constraints, we limited ourselves to 10 (c) and 5 (d) uniformly distributed basis states on the Bloch sphere (with projectors shown in relevant insets).

Apart from addressing the possibility of having no Raman events within a time bin, we also need to account for the possibility of "false positives," i.e., detecting only one of multiple Raman events occurring in a single time bin, due to a photon detection efficiency $\eta < 1$ [59]. The probability of such n-photon false positives, $P_{fp}(n)$, is given by the simple relation

$$\begin{aligned} P_{fp}(n) &= P_{nd}(n) \times P_d(1) \times P_s(n+1) \\ &= C_n^{n+1}(1-\eta)^n \times \eta \times P_s(n+1), \end{aligned} \tag{9}$$

where C_n^{n+1} is the binomial coefficient, $P_d(n)$ [$P_{nd}(n)$] denotes the probability of detecting (not detecting) n photons. We find that $T_B \approx 0.5\ \mu$s remains optimal after taking this into account. Figure 4(d) shows the rate of LC generation for $n = 1$ to 4 for different detector efficiencies.

To demonstrate the robustness of our protocol against nuclear environment fluctuations, we calculate the fidelity between the state obtained with and without Overhauser field (both for the the same set of precession phases determined by randomly chosen scattering times). For a pure hh, only the B_N^z Overhauser component perpendicular to the applied B field affects the protocol [by randomly modifying direction and magnitude of the total B field by $\arctan(B_N^z/B_{\text{ext}})$]. By contrast, a mixed hh-lh system suffers predominantly from the parallel B_N^x component, to an extent determined by the mixing factor α. This is also exemplified in a decreased spin coherence time from the ideal hh limit, as shown in Fig. 4(b). Only considering this term, the following analytical expression (see Appendix E) captures the fidelity decay as a function of T_B:

$$\bar{\mathcal{F}}^{(1)} = \frac{1}{2} + \frac{\sqrt{2\pi}}{4T_B\delta B_N^x}\text{erf}\left(\frac{T_B\delta B_N^x}{\sqrt{2}}\right), \tag{10}$$

where $\bar{\mathcal{F}}^{(n)}$ denotes the average fidelity for a state of n scattered photons [written for $n = 1$ in Eq. (10) above], and δB_N^x is the fluctuation in B_N^x. For a single scattered photon, we obtain $\mathcal{F}_{av}^{(1)} \to \frac{1}{2}$ for large T_B as expected. Not capturing decoherence due to B_N^z fluctuations, Eq. (10) represents an upper bound on the maximally achievable fidelity in the case of finite hh-lh mixing. To fully account for the effects of the stochastically varying net B-field vector, we show numerically obtained [60] fidelity overlaps of desired vs the ensemble-average of realized LC_4 states in Fig. 5. In the presence of the Overhauser field with fluctuations ~14 mT, near unit fidelity remains possible in the region with (moderately) strong $B \gtrsim 0.4$ T and relatively short $T_B \lesssim 0.25\mu$s [Fig. 5(a)]. Conversely, large LC generation rates demand $0.5\ \mu\text{s} \lesssim T_B \lesssim 1\ \mu$s and $B \lesssim 0.1$ T [Fig. 5(b)], so that a tradeoff situation arises. Encouragingly, there is a wide middle ground where high-fidelity operation is possible at respectable rates.

Another important figure of merit of our protocol is the localizable entanglement (LE) [13,61] between any two qubits of the LC state (including the spin). The LE represents the

maximum negativity of the reduced density matrix of two qubits of interest (indexed j and k), after all others have measured out projectively. Choosing the set of projectors $\mathcal{M} = \{P_i : 1 \leqslant i \leqslant n,\ i \notin \{j,k\}\}$ as our measurement defines an ensemble $\mathcal{E}_{\mathcal{M}} := \{p_{\mathcal{M},s}, \rho^{j,k}_{\mathcal{M},s}\}$, where $p_{\mathcal{M},s}$ is the probability of obtaining the two-spin density matrix $\rho^{j,k}_{\mathcal{M},s}$ for the outcome $\{s\}$ having measured the remaining $N-2$ qubits. The LE is then defined as the maximum negativity after averaging over all the outcomes for each measurement, that is,

$$LE^{\mathcal{N}}_{j,k} = \max_{\mathcal{M}} \sum_{s} p_{\mathcal{M},s}\, \mathcal{N}\big(\rho^{j,k}_{\mathcal{M},s}\big), \tag{11}$$

where $\mathcal{N}(\rho^{j,k}_{\mathcal{M},s})$ is the negativity of $\rho^{j,k}_{\mathcal{M},s}$. We choose a quasi-uniformly distributed basis on the Bloch sphere of each qubit [see points in insets of Figs. 5(c) and 5(d)]. The computational unwieldiness of Eq. (11) restricts the number of projectors, and we can only obtain a lower bound of the true LE for $LC_{3,4}$ [Figs. 5(c) and 5(d)]. Within the variance of the sample over which the optimization was performed, the LE falls off with qubit distance, but encouragingly it remains remarkably high overall, and is thus unlikely to be a limiting factor in the length of the LC that could be generated using this protocol.

V. OVERHAUSER FIELD LIMITATIONS

The relatively short T_2^* time of the electron spin due to the fluctuating nuclear environment constitutes a severe shortcoming of real quantum dot spins, putting a limit on the order of a few nanoseconds on any experiment relying on the coherence of this system. For the LR protocol [9] one requires an external field of the order of ∼50 mT along the Y direction in order to obtain a sufficient number of Y gates for a multiphoton $LC_{4\geqslant n\geqslant 2}$ state within a few nanoseconds (assuming instantaneous excitation and radiative decay). Such an applied field, however, activates the previously dipole-forbidden transitions, degrading the correlations between the spin and emitted photons required for the LC state. Applying a strong field results in significant electron-spin precession between the pulsed excitation and spontaneous emission events, reducing the fidelity of the produced LC. By contrast, applying a weaker field limits the scalability of the protocol beyond a string of a couple of photons, as well as failing to screen the effects of the fluctuating Overhauser field. In short, the presence of the Overhauser field implies that the LR protocol would in practice need to be upgraded to incorporate dynamical decoupling and gated Y rotations instead of relying on free spin precession.

One way to overcome some of these hurdles would be to adapt the LR protocol to a hole-spin system, having a longer dephasing time. However, due to the hole spins coupling weakly to external magnetic fields, the precession time would be much longer, requiring stronger fields to implement the Y rotations, hence resulting in the same issue discussed above, namely, the undesirable dipole-forbidden transitions becoming accessible. Shorter coherence times in the presence of a weak external field and phonon sideband emissions (see below) would also be an issue in the hole-spin variant of the LR scheme. Hence, our scheme goes beyond a direct adaptation of the original LR scheme to the hole-spin platform, which would still suffer from most of the shortcomings of the original proposal.

Extending the promising dark exciton (DE) scheme [13] beyond a couple of photons presents similar experimental challenges: the finite radiative lifetime of the biexciton (BiE) $\tau_{\mathrm{BiE}} \approx 0.33$ ns entails that the spin precesses by a non-negligible random amount both in the DE and BiE states, and this limits the purity of the photon polarization state. Furthermore, the DE spin also suffers from environmental decoherence during its precession [13]. It should be noted, however, that the dark exciton scheme proposed in Ref. [13] could be optimized (for example, by using Purcell enhancement) to improve scalability.

The elegant recently proposed scheme in Ref. [10] was designed to be robust against Overhauser fluctuations, provided the scattering events occur on a short enough timescale over which the Overhauser field can be assumed constant (so that only a global phase is gained in each trajectory). However, in this case an additional single-photon source and high cooperativity is required, and any lifting of the selection rules (e.g., due to hole mixing, see below) will still impose practical limitations.

VI. CONCLUSION

We have presented a scheme for generating frequency-encoded LC states, which could serve as a stepping stone towards measurement-based quantum computation. Unlike current rival schemes, our protocol does not rely on the excitation and relaxation of the emitter, and is therefore only sensitive to ground-state hole spin dephasing, at the cost of being limited by its intrinsic probabilistic nature. Based on experimentally informed properties of real epitaxial quantum dots, we have shown that LC states of sufficient length and high fidelity for fusion into larger cluster states can nevertheless be produced at respectable rates. In turn, this facilitates type-II fusing into 2D cluster states [5,62]. Our protocol takes full account of unmitigated Overhauser field fluctuations. It is inherently impervious to hole-mixing-induced modifications of the optical selection rules, but, like other approaches, it stands to gain from dynamic decoupling.

While the probabilistic nature of the Raman scattering events limits our protocol as described in the main text to LC states of length $n < 10$, our approach can, in principle, be made deterministic. The most elegant way of achieving this would be to detect the presence of the Raman scattered photons without absorbing them or learning their frequency, however, this ability does not currently exist for optical photons, which is why we turn to observing the QD spin instead. Continuously monitoring whether a Raman spin flip has happened, but without learning the spin state itself, requires the introduction of a secondary "ancilla" quantum dot as a witness of the spin-photon entangling event. These extensions, discussed in more detail in Appendix H, make the Raman hole-spin emitter a viable, practical alternative in the quest for realizing nonclassical multiphoton states, and importantly one which can be straightforwardly implemented with current expertise and devices.

ACKNOWLEDGMENTS

We thank D. Gershoni, E. Denning, and J. Iles-Smith for insightful and stimulating discussions. D.S. thanks SUPA

for financial support. We acknowledge support from EPSRC (Grant No. EP/M013472/01) and the ERC (Grant No. 307392). B.D.G. thanks the Royal Society for a Wolfson Merit Award, and E.M.G. acknowledges financial support from the Royal Society of Edinburgh and the Scottish Government.

APPENDIX A: SECOND-ORDER PERTURBATION RATE

It can be easily shown that, after moving to a rotating frame with respect to the unperturbed transition frequency, the amplitude of the Raman-flip transition $|\Downarrow\rangle \rightarrow |\Uparrow\rangle$ is given by

$$\mathcal{T}_{\Downarrow\rightarrow\Uparrow} = \frac{\langle\Uparrow;\omega_R|H_I|T_\downarrow;0\rangle\langle T_\downarrow;0|H_I|\Downarrow;\omega_{\mathrm{Ray}}\rangle}{\hbar\Delta_1^{(1)}} + \frac{\langle\Uparrow;\omega_{\mathrm{Ray}}|H_I|T_\uparrow;0\rangle\langle T_\uparrow;0|H_I|\Downarrow;\omega_B\rangle}{\hbar\Delta_2^{(1)}}, \quad \text{(A1)}$$

where $\Delta_1^{(1)} = \delta_h + \delta_e$, $\Delta_2^{(1)} = \delta_h - \delta_e$, H_I is the light-matter interaction Hamiltonian (in this case between the spin and cw laser field), and ω_R, ω_B, and ω_{Ray} are the red- and blue-detuned and Rayleigh scattered photon frequencies, respectively. The first term in Eq. (A1) gives the amplitude of a red Raman photon event: the system, initially in the $|\Downarrow\rangle$ state, scatters a σ^V photon, after which the final state is given by $|\Uparrow;H\rangle$ [that is, the system in the $|\Uparrow\rangle$ state and a red-detuned Raman photon (σ^H polarized) is scattered]. Similarly, the $|\Uparrow\rangle \rightarrow |\Downarrow\rangle$ transition giving rise to the blue-detuned photon scattering event occurs with amplitude

$$\mathcal{T}_{\Uparrow\rightarrow\Downarrow} = \frac{\langle\Downarrow;\omega_B|H_I|T_\uparrow;0\rangle\langle T_\uparrow;0|H_I|\Uparrow;\omega_{\mathrm{Ray}}\rangle}{\hbar\Delta_1^{(2)}} + \frac{\langle\Downarrow;\omega_{\mathrm{Ray}}|H_I|T_\downarrow;0\rangle\langle T_\downarrow;0|H_I|\Uparrow;\omega_R\rangle}{\hbar\Delta_2^{(2)}}, \quad \text{(A2)}$$

where $\Delta_1^{(2)} = -\delta_h - \delta_e$, $\Delta_2^{(2)} = -\delta_h + \delta_e$.

The second term in each of the transition amplitudes does not contribute to the Raman processes, and vanish as the driving field can only drive vertically polarized transitions. After performing the necessary solid angle integrals, we arrive at the scattering rate given by Eq. (8) in the main text.

APPENDIX B: OVERHAUSER FIELD FOR HOLE-SPIN SYSTEMS

Vanishing wave functions at the nuclear sites means that the Fermi-contact hyperfine term for the nuclear–hole-spin interaction is effectively zero, leaving only the dipole-dipole interaction term as the dominant source of dephasing. For an idealized pure hh, this term is of Ising nature, with just the ZZ component being present. In most epitaxially grown QDs, however, some degree of hh $|J;J_z\rangle = |3/2;\pm 3/2\rangle$ and lh $|J;J_z\rangle = |3/2;\pm 1/2\rangle$ mixing is always present [21,63], breaking the Ising-type nature of the dipole-dipole term and introducing XX and YY terms in the Hamiltonian. This means that the eigenstates of the Hamiltonian are no longer given separately by the hh or lh states, but a linear combination of both (the consequences of this mixing in quantum-dot-based LC protocols is further discussed in Appendix F 2). Without going into too much detail, the hyperfine coupling Hamiltonian for the hh-lh states is given by

$$H_{hf}^{dd} = V\sum_j C_j|\Psi(\mathbf{R}_j)|^2\left[\alpha\left(I_x^j S_x + I_y^j S_y\right) + I_z^j S_z\right], \quad \text{(B1)}$$

where C_j are dipole-dipole hyperfine constants, V is the unit-cell volume, and $\alpha = \frac{2}{\sqrt{3}}|\beta|$ is a parameter depending on the deformation potentials for the valence band, and the strain tensor [21,63]. In the "frozen-fluctuation" model [24], this results in an effective magnetic field with mean $\langle\mathbf{B}_N\rangle = (\langle B_N^x\rangle, \langle B_N^y\rangle, \langle B_N^z\rangle)$ (which, due to the finite size of the spin bath, is not necessarily zero), and a fluctuation $\delta\mathbf{B}_N = (\delta B_N^x, \delta B_N^y, \delta B_N^z)$ (which is the source of the spin's loss of coherence), and is assumed to follow normal statistics [21]:

$$P(\mathbf{B}_N) = \left(\frac{1}{2\pi}\right)^{\frac{3}{2}} \frac{1}{\delta B_N^{\parallel 2}\delta B_N^{\perp}} \times \exp\left[-\frac{\Delta B_N^{x\,2}}{2\,\delta B_N^{\parallel 2}} - \frac{\Delta B_N^{y\,2}}{2\,\delta B_N^{\parallel 2}} - \frac{\Delta B_N^{z\,2}}{2\,\delta B_N^{\perp 2}}\right] YY, \quad \text{(B2)}$$

where $\Delta B_N^i = B_N^i - \langle B_N^i\rangle$, $\delta B_N^\perp = \delta B_N^z$, and $\delta B_N^\parallel := \delta B_N^x = \delta B_N^y = \alpha\,\delta B_N^\perp$. Experimentally, Overhauser field fluctuations of 10–30 mT have been measured [26,27], putting a lower-bound on the applied external field required to screen these fluctuations.

APPENDIX C: MATRIX OPERATIONS

Consider a single scattering process that can be described by the action of the product of matrices:

$$\begin{aligned}
|\Uparrow\rangle|\mathrm{Ray}_k\rangle &\rightarrow e^{-i\frac{\phi_1^{(k)}}{2}} e^{i\frac{\phi_2^{(k)}}{2}}(|\Uparrow\rangle + |\Downarrow\rangle)|B_k\rangle \\
&= U_r U_p\left(\phi_2^{(k)}\right) T_s^{(k)} U_p\left(\phi_1^{(k)}\right)|\Uparrow\rangle|\mathrm{Ray}_k\rangle \\
&= Q^{(k)}|\Uparrow\rangle|\mathrm{Ray}_k\rangle, \\
|\Downarrow\rangle|\mathrm{Ray}_k\rangle &\rightarrow e^{i\frac{\phi_1^{(k)}}{2}} e^{-i\frac{\phi_2^{(k)}}{2}}(|\Uparrow\rangle - |\Downarrow\rangle)|R_k\rangle \\
&= U_r U_p\left(\phi_2^{(k)}\right) T_s^{(k)} U_p\left(\phi_1^{(k)}\right)|\Downarrow\rangle|\mathrm{Ray}_k\rangle \\
&= Q^{(k)}|\Downarrow\rangle|\mathrm{Ray}_k\rangle, \quad \text{(C1)}
\end{aligned}$$

where $U_p(\phi_{1,2}^{(k)})$ is the free spin precession transformation before ($\phi_1^{(k)}$) and after ($\phi_2^{(k)}$) the kth scattering event (prior to the $Y_{\frac{\pi}{2}}$ rotation), with the resulting matrix of events being $Q^{(k)} := U_r U_p(\phi_2^{(k)}) T_s^{(k)} U_p(\phi_1^{(k)})$. The scattering matrix $T_s^{(k)}$ is given by

$$T_s^{(k)} = \left(\begin{array}{c|c} 0 & T_R^{(k)} \\ \hline T_B^{(k)} & 0 \end{array}\right), \quad \text{(C2)}$$

with $T_R^{(k)}$ and $T_B^{(k)}$ written in the basis $\{|B_k\rangle, |R_k\rangle, |\mathrm{Ray}_k\rangle\}$, which simultaneously flips the spin state $|\Uparrow\rangle \leftrightarrow |\Downarrow\rangle$, and applies the local transformations

$$\begin{aligned}
T_B^{(k)} &: |\mathrm{Ray}_k\rangle \mapsto |B_k\rangle, \\
T_R^{(k)} &: |\mathrm{Ray}_k\rangle \mapsto |R_k\rangle, \quad \text{(C3)}
\end{aligned}$$

where we have omitted the unaffected photon states for brevity. Hence, $T_B^{(k)}$ and $T_R^{(k)}$ take the form

$$T_R^{(k)} = \mathbb{I}_3^{\otimes_{k-1}} \otimes \begin{pmatrix} 0 & 0 & 0 \\ 0 & 0 & 1 \\ 0 & 0 & 0 \end{pmatrix} \otimes \mathbb{I}_3^{\otimes_{n-k}},$$
$$T_B^{(k)} = \mathbb{I}_3^{\otimes_{k-1}} \otimes \begin{pmatrix} 0 & 0 & 1 \\ 0 & 0 & 0 \\ 0 & 0 & 0 \end{pmatrix} \otimes \mathbb{I}_3^{\otimes_{n-k}}, \tag{C4}$$

and U_r and $U_p(\phi)$ are simply given by given by

$$U_r = \exp\left(i\frac{\pi}{4}\sigma_y\right) \otimes \mathbb{I}_3^{\otimes_n}, \quad U_p(\phi) = \begin{pmatrix} e^{-i\frac{\phi}{2}} & 0 \\ 0 & e^{i\frac{\phi}{2}} \end{pmatrix} \otimes \mathbb{I}_3^{\otimes_n}, \tag{C5}$$

where the first matrices act on the spin state and have been written in the $\{|\Uparrow\rangle, |\Downarrow\rangle\}$ basis. Unfortunately, the matrix product describing n-photon scattering events becomes unwieldy with increasing n. In Appendix D, however, we show that this protocol does indeed generalize to a LC_n state, up to free precession phases.

APPENDIX D: GENERALIZATION TO n PHOTONS

1. Preliminary lemmas

In this section, we will show that the general form of the n-photon state $S^{(n)}$ obtained using our protocol can be written recursively (where we have suppressed the ket representation for these states for ease of notation). In fact, please note:

Lemma 1. $\forall\, n \in \mathbb{N}$, the n-photon state $S^{(n)}$ can be decomposed into the recursive relations

$$S_+^{(n)} = S_+^{(n-1)}|1_n\rangle + S_-^{(n-1)}|0_n\rangle,$$
$$S_-^{(n)} = S_+^{(n-1)}|1_n\rangle - S_-^{(n-1)}|0_n\rangle, \tag{D1}$$

depending whether the spin is measured to be in the $|\Uparrow\rangle$ or $|\Downarrow\rangle$ state, respectively.

Proof. We will, without loss of generality, ignore the spin precession, although the proof is the same for the general case:

Basis case. For $j = 1$, $S_+^{(1)} = |1_1\rangle + |0_1\rangle$ and $S_-^{(1)} = |1_1\rangle - |0_1\rangle$. After the next scattering event, we get

$$\begin{aligned} S_+^{(2)} &= |1_1 1_2\rangle + |1_1 0_2\rangle + |0_1 1_2\rangle - |0_1 0_2\rangle \\ &= (|1_1\rangle + |0_1\rangle)|1_2\rangle + (|1_1\rangle - |0_1\rangle)|0_2\rangle \\ &= S_+^{(1)}|1_2\rangle + S_-^{(1)}|0_2\rangle. \end{aligned} \tag{D2}$$

Similarly,

$$\begin{aligned} S_-^{(2)} &= |1_1 1_2\rangle - |1_1 0_2\rangle + |0_1 1_2\rangle + |0_1 0_2\rangle \\ &= (|1_1\rangle + |0_1\rangle)|1_2\rangle - (|1_1\rangle - |0_1\rangle)|0_2\rangle \\ &= S_+^{(1)}|1_2\rangle - S_-^{(1)}|0_2\rangle. \end{aligned} \tag{D3}$$

Induction step. Assume statement holds for $j = n$, and consider the $(n+1)$th scattering event:

$$\begin{aligned} S_+^{(n+1)} &= U_r T_{\mathrm{scat}}^{(n+1)}(|\Uparrow\rangle S_+^{(n)} + |\Downarrow\rangle S_-^{(n)})|\mathrm{Ray}_{n+1}\rangle \\ &= (|\Uparrow\rangle + |\Downarrow\rangle)S_+^{(n)}|1_{n+1}\rangle + (|\Uparrow\rangle - |\Downarrow\rangle)S_-^{(n)}|0_{n+1}\rangle \\ &= |\Uparrow\rangle(S_+^{(n)}|1_{n+1}\rangle + S_-^{(n)}|0_{n+1}\rangle) \\ &\quad + |\Downarrow\rangle(S_+^{(n)}|1_{n+1}\rangle - S_-^{(n)}|0_{n+1}\rangle). \end{aligned} \tag{D4}$$

Therefore, $S_+^{(n+1)} = S_+^{(n)}|1_{n+1}\rangle + S_-^{(n)}|0_{n+1}\rangle$ and $S_-^{(n+1)} = S_+^{(n)}|1_{n+1}\rangle - S_-^{(n)}|0_{n+1}\rangle$, so the statement holds $\forall\, n \in \mathbb{N}$. ■

It is then easy to see that we also have the following:

Lemma 2.

$$\sigma_z^{(n)} S_\pm^{(n)} = -S_\mp^{(n)} \quad \forall\, n \in \mathbb{N}, \tag{D5}$$

which we shall use to prove that the n-photon state we generate is indeed a linear cluster state.

2. Equivalence to LC_n states

In order to show that the $S_\pm^{(n)}$ states are indeed LC_n's, we have to show that they both satisfy the set of eigenvalue equations

$$K_n^{(a)} S_\pm^{(n)} = (-1)^{k_\pm^{(a)}} S_\pm^{(n)}, \tag{D6}$$

with

$$K_n^{(a)} = \sigma_x^{(a)} \bigotimes_{b \in N(a)} \sigma_z^{(b)}, \tag{D7}$$

where $1 \leqslant a \leqslant n$, $N(a)$ is the set of direct neighbors of photon a along the state, and $k_\pm^{(a)} \in \{0, 1\}$, depending on the particular realization of LC_n. The subscript on the operator K denotes the state tensor length of K, and hence the length of the state it acts upon. In fact, we shall show the following statement:

Theorem 1. The n-photon $S^{(n)}$ state satisfies the set of LC_n-eigenvalue equations for

$$k_+^{(a)} = \begin{cases} 1, & \text{if } a \in \{1, n\} \\ 0, & \text{if } 1 < a < n \end{cases}$$
$$k_-^{(a)} = \begin{cases} 1, & \text{if } a = 1 \\ 0, & \text{if } 1 < a \leqslant n. \end{cases} \tag{D8}$$

Proof. The proof follows, once again, by induction, as well as the use of Lemma 1.

Basis case. For $j = 2$,

$$\begin{aligned} S_+^{(2)} &= (|1_1\rangle + |0_2\rangle)|1_n\rangle + (|1_1\rangle - |0_1\rangle)|0_2\rangle, \\ S_+^{(2)} &= (|1_1\rangle + |0_2\rangle)|1_n\rangle - (|1_1\rangle - |0_1\rangle)|0_2\rangle, \end{aligned} \tag{D9}$$

and the statement holds when applying $\sigma_x^{(1)} \otimes \sigma_z^{(2)}$ and $\sigma_z^{(1)} \otimes \sigma_x^{(2)}$.

Induction step. Suppose the statement holds for $j = n$, and consider $S_+^{(n+1)} = S_+^{(n)}|1_{n+1}\rangle + S_-^{(n)}|0_{n+1}\rangle$. Then,

If $a = 1$,

$$\begin{aligned} K_{n+1}^{(a)} S_+^{(n+1)} &= \left(K_n^{(a)} \otimes \mathbb{I}_2\right)(S_+^{(n)}|1_{n+1}\rangle + S_-^{(n)}|0_{n+1}\rangle) \\ &= (-1)^{k_+^{(1)}} S_+^{(n)}|1_{n+1}\rangle + (-1)^{k_-^{(1)}} S_-^{(n)}|0_{n+1}\rangle \\ &= -(S_+^{(n)}|1_{n+1}\rangle + S_-^{(n)}|0_{n+1}\rangle) \\ &= -S_+^{(n+1)}, \end{aligned} \tag{D10}$$

with $\mathbb{I}_2$ being the 2×2 identity matrix. The penultimate step holds due the induction hypothesis. Similarly, for $S_-^{(n+1)}$,

$$\begin{aligned} K_{n+1}^{(a)} S_-^{(n+1)} &= \left(K_n^{(a)} \otimes \mathbb{I}_2\right)(S_+^{(n)}|1_{n+1}\rangle - S_-^{(n)}|0_{n+1}\rangle) \\ &= (-1)^{k_+^{(1)}} S_-^{(n)}|1_{n+1}\rangle - (-1)^{k_-^{(1)}} S_-^{(n)}|0_{n+1}\rangle \\ &= -(S_+^{(n)}|1_{n+1}\rangle - S_-^{(n)}|0_{n+1}\rangle) = -S_-^{(n+1)}. \end{aligned} \tag{D11}$$

If $1 < a < n$,

$$\begin{aligned} K_{n+1}^{(a)} S_+^{(n+1)} &= \left(K_n^{(a)} \otimes \mathbb{I}_2\right)\left(S_+^{(n)}|1_{n+1}\rangle + S_-^{(n)}|0_{n+1}\rangle\right) \\ &= (-1)^{k_+^{(a)}} S_+^{(n)}|1_{n+1}\rangle + (-1)^{k_-^{(a)}} S_-^{(n)}|0_{n+1}\rangle \\ &= S_+^{(n)}|1_{n+1}\rangle + S_-^{(n)}|0_{n+1}\rangle \\ &= S_+^{(n+1)}, \end{aligned} \tag{D12}$$

$$\begin{aligned} K_{n+1}^{(a)} S_-^{(n+1)} &= \left(K_n^{(a)} \otimes \mathbb{I}_2\right)\left(S_+^{(n)}|1_{n+1}\rangle - S_-^{(n)}|0_{n+1}\rangle\right) \\ &= (-1)^{k_+^{(a)}} S_-^{(n)}|1_{n+1}\rangle - (-1)^{k_-^{(a)}} S_-^{(n)}|0_{n+1}\rangle \\ &= S_+^{(n)}|1_{n+1}\rangle - S_-^{(n)}|0_{n+1}\rangle \\ &= S_-^{(n+1)}. \end{aligned} \tag{D13}$$

If $a = n$,

$$\begin{aligned} K_{n+1}^{(a)} S_+^{(n+1)} &= \left(K_n^{(a)} \otimes \sigma_z^{(n+1)}\right)\left(S_+^{(n)}|1_{n+1}\rangle + S_-^{(n)}|0_{n+1}\rangle\right) \\ &= -(-1)^{k_+^{(n)}} S_+^{(n)}|1_{n+1}\rangle + (-1)^{k_-^{(n)}} S_-^{(n)}|0_{n+1}\rangle \\ &= S_+^{(n)}|1_{n+1}\rangle + S_-^{(n)}|0_{n+1}\rangle \\ &= S_+^{(n+1)}, \end{aligned} \tag{D14}$$

$$\begin{aligned} K_{n+1}^{(a)} S_-^{(n+1)} &= \left(K_n^{(a)} \otimes \sigma_z^{(n+1)}\right)\left(S_+^{(n)}|1_{n+1}\rangle - S_-^{(n)}|0_{n+1}\rangle\right) \\ &= -(-1)^{k_+^{(n)}} S_-^{(n)}|1_{n+1}\rangle - (-1)^{k_-^{(n)}} S_-^{(n)}|0_{n+1}\rangle \\ &= S_+^{(n)}|1_{n+1}\rangle - S_-^{(n)}|0_{n+1}\rangle \\ &= S_-^{(n+1)}. \end{aligned} \tag{D15}$$

For the $a = n+1$ case, we shall make use of Lemma 2. The operator $K_{n+1}^{(n+1)}$ can be decomposed as $\mathbb{I}_2^{\otimes_{n-1}} \otimes \sigma_z^{(n)} \otimes \sigma_x^{(n+1)}$, and hence we get the following:

If $a = n+1$,

$$\begin{aligned} K_{n+1}^{(a)} S_+^{(n+1)} &= -S_-^{(n)}|0_{n+1}\rangle - S_+^{(n)}|1_{n+1}\rangle \\ &= -S_+^{(n+1)}, \end{aligned} \tag{D16}$$

$$\begin{aligned} K_{n+1}^{(a)} S_-^{(n+1)} &= -S_-^{(n)}|0_{n+1}\rangle + S_+^{(n)}|1_{n+1}\rangle \\ &= S_-^{(n+1)}. \end{aligned} \tag{D17}$$

Therefore, the states $S_\pm^{(n)}$ satisfy the eigenvalue conditions (D6) for the set of parameters (D8), meaning that the state obtained by our protocol is an LC_n state. ■

APPENDIX E: AVERAGE FIDELITY

Consider a single scattering event in which the spin precesses for a time $T_B^{(1)}$ prior to the scattering event and a subsequent precession time $T_B^{(2)}$ followed by a Y rotation marking the end of the run (such that $T_B^{(1)} + T_B^{(2)} = T_B$). In the presence of the B_N^x component, the rotation matrix $U_p(\phi)$ in (C5) picks up a stochastic term $\omega_N t$, that is,

$$U_p((\omega_B + \omega_N)t) = \begin{pmatrix} e^{-i\frac{1}{2}(\omega_B+\omega_N)t} & 0 \\ 0 & e^{i\frac{1}{2}(\omega_B+\omega_N)t} \end{pmatrix} \otimes \mathbb{I}_3^{\otimes_n}, \tag{E1}$$

with $t = T_B^{(1)}$ or $T_B^{(2)}$, where we have written the precessed angle explicitly in terms of $\omega_B = g_h^x \mu_B B_{\mathrm{ext}}/\hbar$ and the Overhauser stochastic frequency $\omega_N = g_h^x \mu_B B_N^x/\hbar$ (g_h^x being the x component of the anisotropic hole g factor [64]).

The effect of this stochastic term can be seen in the trace fidelity between post Y rotation ideal photon state, and the more realistic case including the Overhauser field. The spin+photon states for the two cases, denoted by $S^{(1)}$ and $\tilde{S}^{(1)}$, respectively, are then given by

$$\begin{aligned} S^{(1)} &= e^{-i\frac{1}{2}\omega_B \delta T_B}|\Uparrow B_1\rangle + e^{-i\frac{1}{2}\omega_B \delta T_B}|\Downarrow B_1\rangle \\ &\quad + e^{i\frac{1}{2}\omega_B \delta T_B}|\Uparrow R_1\rangle - e^{i\frac{1}{2}\omega_B \delta T_B}|\Downarrow R_1\rangle, \\ \tilde{S}^{(1)} &= e^{-i\frac{1}{2}(\omega_B+\omega_N)\delta T_B}|\Uparrow B_1\rangle + e^{-i\frac{1}{2}(\omega_B+\omega_N)\delta T_B}|\Downarrow B_1\rangle \\ &\quad + e^{i\frac{1}{2}(\omega_B+\omega_N)\delta T_B}|\Uparrow R_1\rangle - e^{i\frac{1}{2}(\omega_B+\omega_N)\delta T_B}|\Downarrow R_1\rangle, \end{aligned} \tag{E2}$$

where $\delta T_B = T_B^{(1)} - T_B^{(2)} \in [-T_B, T_B]$ is a uniform random variable due to the fact that the spin precesses multiple times during T_B in the high external magnetic field. The final photon state, as discussed earlier, depends on the state the spin is measured in, so we shall denote the density matrices of the ideal and realistic cases by $\rho_+^{(1)}$ and $\xi_+^{(1)}$, respectively, if the spin is measured in the $|\Uparrow\rangle$ state, and similarly $\rho_-^{(1)}$ and $\xi_-^{(1)}$ for the $|\Downarrow\rangle$ result. The fidelity for a fixed value of B_N^x is then given by $\mathcal{F}^{(1)} = \mathrm{tr}(\rho_+^{(1)}\xi_+^{(1)}) = \mathrm{tr}(\rho_-^{(1)}\xi_-^{(1)}) = \cos^2(B_N^x \delta T_B/2)$.

Due to the stochastic nature of the Overhauser field, we need to ensemble average $\mathcal{F}^{(1)}$ in order to get the true fidelity, that is, $\bar{\mathcal{F}}^{(1)} = \langle\langle \mathrm{tr}(\rho_-^{(1)}\xi_-^{(1)})\rangle_B\rangle_{\delta T} = \langle\langle \mathrm{tr}(\rho_+^{(1)}\xi_+^{(1)})\rangle_B\rangle_{\delta T}$, where the Overhauser averaging $\langle\ldots\rangle_B$ and time averaging $\langle\ldots\rangle_{\delta T}$ are performed over a normal distribution with zero mean and finite standard deviation δB_N^x, and a uniform distribution over $[-T_B, T_B]$ [65]. In doing so, we get the averaged fidelity for a single scattering event in the presence of B_N^x given by Eq. (10).

APPENDIX F: IMPERFECTIONS OF OTHER QD-BASED PROTOCOLS

As discussed in the main text, several protocols have been proposed for implementing photonic LC states or entangled states sharing similar properties. The influential 2009 proposal by Lindner and Rudolph [9] (LR) offered an elegant and simple scheme which could be implemented using the circularly polarized degrees of freedom of a quantum dot. Despite its simplicity, a number of experimental barriers need to be overcome to actually implement such a scheme. The Overhauser fluctuation limitations have already been discussed in the main text; below we discuss some additional constraints both for the LR scheme as well as the recent dark exciton (DE) based LC scheme [13], which has already successfully produced LC_2 states in the laboratory and shown promise for reaching up to LC_5. In essence, these imperfections effectively introduce limits to the size of achievable cluster states for those protocols, hence limiting the indefinite deterministic operation in the absence of further optimizations. By contrast, we note that our approach in this work, as discussed in the main paper, is largely immune against all issues discussed below.

1. Shortcomings due to coupling to phonons

The solid-state environment further limits the deterministic nature of these protocols due to coupling to the phonon environment. Even in the limit of idealized instantaneous excitation pulses, a temperature-dependent fraction of the photons are inevitably emitted incoherently via the phonon sideband (∼9% at temperatures as low as $T = 4$ K, increasing with temperature [66]). This affects all protocols involving electronic excitation to trion of biexciton states, i.e., both the LR and DE approaches.

2. Effects of hole-state mixing

In this section, we discuss how said protocols fare against finite hh-lh mixing [67]. The first type of hh-lh mixing, due to anisotropy in the in-plane strain of the quantum dot, gives rise to the hh ↑ -lh ↓ mixing, resulting in the hole eigenstates

$$|\Uparrow\rangle = \frac{1}{\sqrt{1+|\beta_{ud}|^2}}(|3/2;+3/2\rangle + \beta_{ud}|3/2;-1/2\rangle),$$
$$|\Downarrow\rangle = \frac{1}{\sqrt{1+|\beta_{ud}|^2}}(|3/2;-3/2\rangle + \beta^*_{ud}|3/2;+1/2\rangle), \quad \text{(F1)}$$

where, without giving its explicit form, β_{ud} is the in-plane strain-dependent mixing factor [21,63]. This type of mixing primarily causes ellipticity of the dipole-allowed transitions which, for a hh system, would be driven by $\sigma^{\pm}$-polarized light. Hence, this hh ↑ -lh ↓ mixing does not induce the "diagonal" dipole-forbidden transitions.

On the other hand, the hh ↑ -lh ↑ mixing may allow transitions which would otherwise be forbidden for a hh system. The hole eigenstates solely due to this type of mixing are given by

$$|\Uparrow\rangle = \frac{1}{\sqrt{1+|\beta_{uu}|^2}}(|3/2;+3/2\rangle + \beta_{uu}|3/2;+1/2\rangle),$$
$$|\Downarrow\rangle = \frac{1}{\sqrt{1+|\beta_{uu}|^2}}(|3/2;-3/2\rangle + \beta^*_{uu}|3/2;-1/2\rangle), \quad \text{(F2)}$$

where β_{uu} is the hh ↑ -lh ↑ admixture factor [21,63]. From Eqs. (F2), it can be immediately seen that the transitions, which are forbidden in Faraday geometry, are now allowed. For hole spins, β_{uu} has been measured to be ∼8%, leading to allowed-to-forbidden transition ratios of $|\beta_{uu}|^2/3 \approx 0.2\%$ [63], although this varies from one quantum dot to another. This means that even if the external field in the LR scheme is weak enough to preserve a pure Faraday geometry, dipole-forbidden transitions may still occur with some small, but finite probability, both for the original and the hole-spin variant of the LR protocol.

Similarly, in the DE system z-polarized "forbidden" transitions are also present due to hole subband mixing, although these transitions in this system are significantly weaker [68,69]. In addition to hh-lh mixing, the DE scheme also suffers from dark-bright exciton (DE-BE) state mixing due to the breaking of the C_{2v} symmetry, although this effect is much weaker than the hh-lh mixing. Realistically, self-assembled QDs suffer from a reduction in symmetry during the growth process, causing a departure from the ideal C_{2v} symmetry. The resulting "reduced" C_s symmetry leads to DE-BE state couplings of two kinds; the first leads to finite z-polarized dipole transitions similar to the hh ↑ -lh ↓ admixture in the BE schemes, while the second gives rise to forbidden in-plane transitions, bearing similar repercussions as the hh ↑ -lh ↑ mixing discussed above [68,70], although to a much lesser extent.

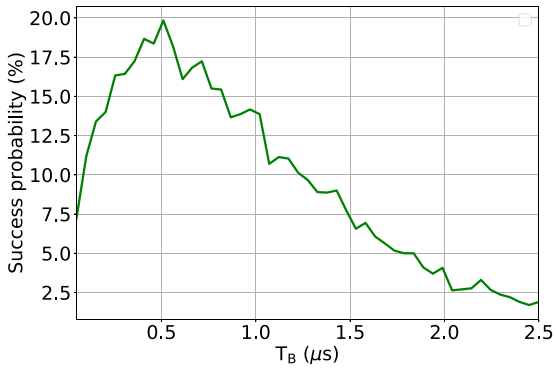

FIG. 6. Success probability of scattering a single Raman photon using a cw source against time-bin length T_B. At an optimized time-bin length $T_B \approx 0.5$ μs, the probability can be as high as 20%, before it drops once more due to the probabilities of getting multiple photons in a single time bin.

We note that our approach does not suffer from modifications of the selection rules due to hole mixing: we already rely on the presence of off-diagonal transitions and slight changes to their rates will not make an appreciable difference.

3. Pulsed scheme limitations

As mentioned earlier, the main limitation of our scheme is the unknown time of arrival of the photons due to the cw source. An obvious solution might be using a pulsed source for the photons. Despite addressing the issue of the photons' unknown phases, such a protocol would still not be deterministic, as there is still a 50% probability that a Rayleigh scattering event, instead of a spin-flipping Raman one, occurs. While this is still a considerable improvement over the ∼20% we get for an optimized time-bin length (Fig. 6), this pulsed-excitation scheme would not benefit from the advantages of subsaturation driving, mainly, the photon linewidth limited only by the hole-spin coherence and laser linewidth, and be susceptible to phonon dephasing. Hence, the opportunity to create longer LCs with less probabilistic phase uncertainty comes at the price of lower quality LC states, which we argue is paramount for reliably constructing 2D cluster states required for quantum computation using probabilistic fusion gates.

APPENDIX G: ROBUSTNESS OF 2D CLUSTER-STATE PROTOCOLS AND LC STATE FUSING SCHEMES

Schemes extending the LR scheme for 2D cluster state generation have been proposed [17], in which it was shown that a pair of entangled QDs could be used to directly generate a 2D cluster state, reducing the required number of probabilistic fusion of LC state building blocks. Furthermore, it was recently shown that the requirement of two-qubit gates on the entangling emitters can be relaxed by a careful application of pulses and single-qubit gates on the emitters [18]. However, building on a similar setup and selection rules as the original

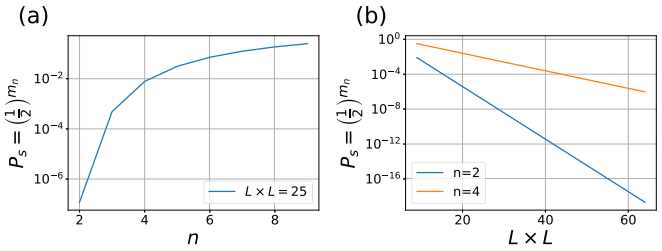

FIG. 7. (a) Success probability of obtaining a 5×5 2D cluster state as a function of the length of the input LC states to be fused. Going from LC_2 to LC_4 shows orders-of-magnitude improvement, underlining that having at least moderately sized LC states is essential for feasible 2D state growth. (b) Success probability against 2D cluster state size for LC_2 (bottom, blue line) and LC_4 (top, orange line) "building blocks," showing an increased improvement with size when going from one-dimensional states of size 2 to size 4.

LR protocol, we expect that the practical limitations discussed above will also limit the achievable size of photonic states that can be obtained with this protocol.

An alternative approach to generating a 2D cluster state is that of fusing LC states. We show that having high-fidelity LC states of moderate length is essential for using one-dimensional states as building blocks. Consider a 2D cluster state of size $L \times L$. If we start with number of linear cluster states of size n, then the number of steps required to at least reach a 2D cluster state of size $L \times L$ is at least $m_n = \frac{L^2-n}{n-1}$: assuming that we have enough linear clusters to start with, each fusion process will (on average) increase the cluster size by $n(m_n + 1) - m_n$ (noting that each fusion step leaves the fused qubit redundantly encoded with two photons in type-II fusion, and disregarding the final layout of the 2D state for generality and simplicity). Clearly, we ignore the cases when $n > L^2$ as the probability saturates for $n = L^2$. We show how the probability scales for a 2D cluster state of size 5×5 as a function of the "building block" size (i.e., the size of the initial cluster states) in Fig. 7(a). This clearly demonstrates that the probability increases exponentially before saturating, showing a significant jump when going from linear cluster sizes of 2 to 4.

This increase in success probability is further emphasized when one considers increasing the 2D cluster state size. In Fig. 7(b), we show how the difference in probability increases with increasing 2D state size $L \times L$. This approach assumes that upon failure, we have enough resources to replace the linear cluster state and try again. The results of this relatively naïve and basic analysis are further backed by an alternative approach presented in Ref. [71], in which Gross *et al.* fuse linear clusters by "weaving" $n + 1$ linear clusters of size n to form a cluster state of size $n \times n$. They show that as long as a careful choice of parameters is made, depending on the fusion success probability, then the cluster state can be prepared using $O(n^2)$ edges and the overall success probability approaches unity as n goes to infinity.

Aside from having relatively longer linear states as building blocks, the fidelity of these states, indicative of quality, is also an important factor when considering scalability to higher dimensions [62,72], as it will determine the "percolation" or "edge-bound" probability. Fortunately, our approach can deliver on both counts by producing LC_4 states with high fidelity at a respectable generation rate.

APPENDIX H: PROPOSAL FOR DETERMINISTIC SCHEME USING DQD

Motivated by recent theoretical and experimental work, we propose extending our Raman protocol to a double quantum dot (DQD) system, where, depending on the relative strength of the exchange interaction and transition energy detuning between the two QDs, either joint measurements on the DQD system can be performed, while leaving the photon-entangling hole-spin state unaffected, or oscillations between joint states can be detected without collapsing the system joint state. In the following, we will discuss two possibilities of extending our protocol in such a way.

(a) *Electrical control*. During the past few years, great progress has been made in synthesizing and controlling quantum dot molecules, both in stacked [73–75] and lateral [76,77] geometries. A Raman-spin flip DQD scheme was shown in Ref. [78], in which the external field is applied in Faraday geometry and the Raman spin flips occur between the singlet S and triplet T_0 states of the system. While this configuration would not allow screening of the dominant fluctuation component of the Overhauser field, such a setup would, in principle, allow a current measurement scheme to be applied and signal the Raman events. In fact, the standard singlet-triplet spin blockade used in gated DQDs [79] could be used to detect current drops, signaling the Raman event. This would require operation round the (1,0), (1,1), (2,0) triple point at a negative bias, making use of the the additional charge state $S(2, 0)$. Addressing and manipulation of these singlet and triplet states in optically active DQDs have been recently been demonstrated for QD molecules [75,78,80–82], whereas the current transport measurements have been long understood for surface-defined QDs. This route would require a hybrid gated and optically active device, which, although certainly challenging, might nonetheless present a feasible route.

(b) *Optical control*. A more attractive alternative to having a gated structure would be to have an all-optical noninvasive spin readout technique, provided by the rich energy-level structure for these systems. In quantum dot molecules, this can be achieved by using the distributed trion state, with the ancilla spin being empty, while the host spin being singly electron charged. The spin readout technique was demonstrated experimentally performing resonance fluorescence (RF) on the $|\downarrow_s, 0_a\rangle \leftrightarrow |\downarrow_s, \downarrow \Uparrow_a\rangle$ transition, which is decoupled from the main spin-flip transition [83]. This technique could be readily extended to hole-spin systems with an analogous level structure. A similar setup was demonstrated experimentally in Ref. [84], where use of these cycling transitions was made to detect the flips of the host spin state. Both these setups would require individual addressing of the ancilla and host spin, meaning that the two QDs selected must be sufficiently relatively far detuned, which could be achieved by tuning the bias voltage over the sample, decreasing the exchange energy splitting [80]. Alternatively, for samples with a much stronger singlet-triplet splitting, optical addressing of the joint states would be more feasible. In the singlet-triplet Raman scheme

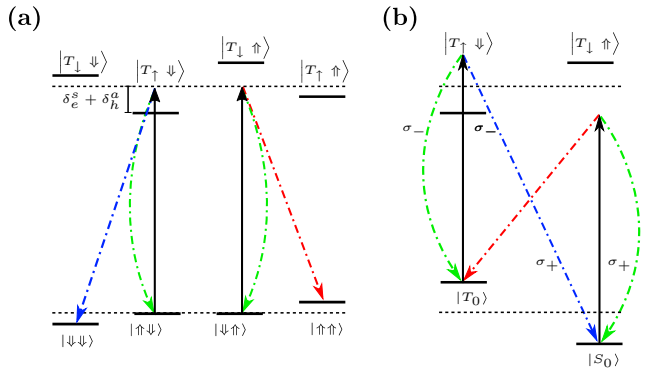

FIG. 8. (a) Extending the Raman spin-flip protocol to a DQD setup in Voigt geometry, where the two QDs are sufficiently detuned (relative to the exchange interaction), allowing the optical addressing of a single spin. (b) An alternative setup in Faraday geometry [78], in which the initial state would be a superposition of S and T_0 states.

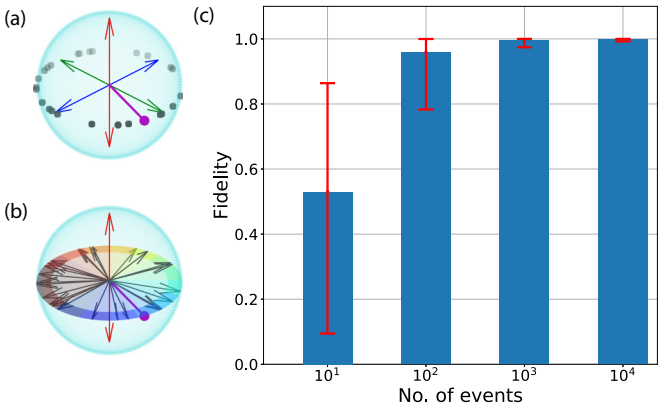

FIG. 9. (a) Bloch sphere representation of the problem: the actual state to be reconstructed (purple) gains a random phase (dots) prior to every measurement, with the measurement bases given by the arrows. (b) An equivalent picture where the state is fixed, with the "random" measurement basis given by the phases. (c) Fidelity for 16 grouped projectors, showing, as expected, an increase in the fidelity for higher numbers of events.

in Faraday geometry discussed in Ref. [78] [Fig. 8(b)], spin readout of the singlet state can be performed by using the decoupled cycling transition $T_+ \leftrightarrow R_{++}$ [81].

APPENDIX I: QUANTUM STATE TOMOGRAPHY

Quantum state tomography (QST) allows one to completely characterize an unknown quantum state, as long as an ensemble of identical copies of such a state can be created in the experiment. Despite the wide range of tomographic techniques in existence [85–87], the aim is typically to use sets of repeated measurements on the ensemble, the results of which enable the reconstruction of the original state.

Our probabilistic protocol then presents an obvious question as to how would one obtain multiple copies of the cluster state since, for each realization, the phases imprinted on the photonic qubits are random, and are only know post detection. Using conventional reconstruction techniques would then average over the coherences of the cluster state, losing the entanglement information.

Despite this apparent downfall, the fact that the random phases can be determined post measurement means that this problem can be reformulated in a "static frame" with respect to the state, that is, the state is not imprinted with the phases, instead, in this frame, the effective basis chosen for the actual measurement rotates for each measurement due to the different phases. The problem then reduces to reconstructing a state when the measurement basis used is different for each measurement. We emphasize that this does not mean that the experimentally chosen basis is actually rotated for each measurement. The random measurement projectors can then be grouped as $\{P_1^{(j)}, P_2^{(j)}, \ldots, P_{n_j}^{(j)}\}$ by proximity on the Bloch sphere into projectors $\{\mathcal{P}_j : 1 \leqslant j \leqslant K\}$ to be used for reconstruction.

As a proof of principle, we used the state $c_1|H\rangle + c_2|V\rangle$ for each experiment, where c_1 and c_2 are two random complex numbers, so that each time we have a different measurement projector. Using maximum likelihood estimation (MLE) and the Cholesky decomposition for the density matrix, we performed QST for various numbers of grouped projectors, the results of which are shown in Fig. 9. As the number of of $\mathcal{P}_j$ is increased, the fidelity rises, as expected. However, for lower numbers of events, the fidelity peaks at a number of grouped projectors, and then starts declining again. This drop is due to the failure of the Gaussian assumption used for MLE. This failure is expected to affect fidelities for higher event numbers as we increase the number of projectors.

[1] H. J. Briegel and R. Raussendorf, Persistent Entanglement in Arrays of Interacting Particles, Phys. Rev. Lett. **86**, 910 (2001).

[2] R. Raussendorf and H. J. Briegel, A One-Way Quantum Computer, Phys. Rev. Lett. **86**, 5188 (2001).

[3] R. Raussendorf, J. Harrington, and K. Goyal, Topological fault-tolerance in cluster state quantum computation, New J. Phys. **9**, 199 (2007).

[4] J. L. O'Brien, A. Furusawa, and J. Vuckovic, Photonic quantum technologies, Nat. Photonics **3**, 687 (2009).

[5] D. E. Browne and T. Rudolph, Resource-Efficient Linear Optical Quantum Computation, Phys. Rev. Lett. **95**, 010501 (2005).

[6] D. A. Herrera-Martí, A. G. Fowler, D. Jennings, and T. Rudolph, Photonic implementation for the topological cluster-state quantum computer, Phys. Rev. A **82**, 032332 (2010).

[7] Y. S. Weinstein, Fusing imperfect photonic cluster states, J. Mod. Opt. **58**, 1285 (2011).

[8] M. A. Nielsen, Optical Quantum Computation Using Cluster States, Phys. Rev. Lett. **93**, 040503 (2004).

[9] N. H. Lindner and T. Rudolph, Proposal for Pulsed On-Demand Sources of Photonic Cluster State Strings, Phys. Rev. Lett. **103**, 113602 (2009).

[10] E. V. Denning, J. Iles-Smith, D. P. S. McCutcheon, and J. Mørk, Protocol for generating multiphoton entangled states from quantum dots in the presence of nuclear spin fluctuations, Phys. Rev. A **96**, 062329 (2017).

[11] S. D. Barrett and P. Kok, Efficient high-fidelity quantum computation using matter qubits and linear optics, Phys. Rev. A **71**, 060310 (2005).

[12] Z.-R. Lin, G.-P. Guo, T. Tu, F.-Y. Zhu, and G.-C. Guo, Generation of Quantum-Dot Cluster States with a Superconducting Transmission Line Resonator, Phys. Rev. Lett. **101**, 230501 (2008).

[13] I. Schwartz, D. Cogan, E. R. Schmidgall, Y. Don, L. Gantz, O. Kenneth, N. H. Lindner, and D. Gershoni, Deterministic generation of a cluster state of entangled photons, Science **354**, 434 (2016).

[14] S. E. Economou and P. Dev, Spin-photon entanglement interfaces in silicon carbide defect centers, Nanotechnology **27**, 504001 (2016).

[15] G. Vallone, E. Pomarico, P. Mataloni, F. De Martini, and V. Berardi, Realization and Characterization of a Two-Photon Four-Qubit Linear Cluster State, Phys. Rev. Lett. **98**, 180502 (2007).

[16] X. Zou and W. Mathis, Generating a four-photon polarization-entangled cluster state, Phys. Rev. A **71**, 032308 (2005).

[17] S. E. Economou, N. Lindner, and T. Rudolph, Optically Generated 2-Dimensional Photonic Cluster State from Coupled Quantum Dots, Phys. Rev. Lett. **105**, 093601 (2010).

[18] M. Gimeno-Segovia, T. Rudolph, and S. E. Economou, Deterministic generation of large-scale entangled photonic cluster state from interacting solid state emitters, arXiv:1801.02599.

[19] J. Iles-Smith, D. P. S. McCutcheon, A. Nazir, and J. Mørk, Phonon scattering inhibits simultaneous near-unity efficiency and indistinguishability in semiconductor single-photon sources, Nat. Photonics **11**, 521 (2017).

[20] A. V. Khaetskii, D. Loss, and L. Glazman, Electron Spin Decoherence in Quantum Dots Due to Interaction with Nuclei, Phys. Rev. Lett. **88**, 186802 (2002).

[21] C. Testelin, F. Bernardot, B. Eble, and M. Chamarro, Hole-spin dephasing time associated with hyperfine interaction in quantum dots, Phys. Rev. B **79**, 195440 (2009).

[22] J. Hansom, C. H. H. Schulte, C. Le Gall, C. Matthiesen, E. Clarke, M. Hugues, J. M. Taylor, and M. Atatüre, Environment-assisted quantum control of a solid-state spin via coherent dark states, Nat. Phys. **10**, 725 (2014).

[23] R. N. E. Malein, T. S. Santana, J. M. Zajac, A. C. Dada, E. M. Gauger, P. M. Petroff, J. Y. Lim, J. D. Song, and B. D. Gerardot, Screening Nuclear Field Fluctuations in Quantum Dots for Indistinguishable Photon Generation, Phys. Rev. Lett. **116**, 257401 (2016).

[24] I. A. Merkulov, Al. L. Efros, and M. Rosen, Electron spin relaxation by nuclei in semiconductor quantum dots, Phys. Rev. B **65**, 205309 (2002).

[25] P. F. Braun, X. Marie, L. Lombez, B. Urbaszek, T. Amand, P. Renucci, V. K. Kalevich, K. V. Kavokin, O. Krebs, P. Voisin, and Y. Masumoto, Direct Observation of the Electron Spin Relaxation Induced by Nuclei in Quantum Dots, Phys. Rev. Lett. **94**, 116601 (2005).

[26] E. A. Chekhovich, M. N. Makhonin, A. I. Tartakovskii, A. Yacoby, H. Bluhm, K. C. Nowack, and L. M. K. Vandersypen, Nuclear spin effects in semiconductor quantum dots, Nat. Mater. **12**, 494 (2013).

[27] B. Urbaszek, X. Marie, T. Amand, O. Krebs, P. Voisin, P. Maletinsky, A. Högele, and A. Imamoğlu, Nuclear spin physics in quantum dots: An optical investigation, Rev. Mod. Phys. **85**, 79 (2013).

[28] L. Viola, E. Knill, and S. Lloyd, Dynamical Decoupling of Open Quantum Systems, Phys. Rev. Lett. **82**, 2417 (1999).

[29] W. M. Witzel and S. Da Sarma, Concatenated dynamical decoupling in a solid-state spin bath, Phys. Rev. B **76**, 241303 (2007).

[30] W. Zhang, V. V. Dobrovitski, L. F. Santos, L. Viola, and B. N. Harmon, Dynamical control of electron spin coherence in a quantum dot: A theoretical study, Phys. Rev. B **75**, 201302 (2007).

[31] G. S. Uhrig, Keeping a Quantum Bit Alive by Optimized π-Pulse Sequences, Phys. Rev. Lett. **98**, 100504 (2007).

[32] G. S. Uhrig, Exact results on dynamical decoupling by pulses in quantum information processes, New J. Phys. **10**, 083024 (2008).

[33] H. Bluhm, S. Foletti, I. Neder, M. Rudner, D. Mahalu, V. Umansky, and A. Yacoby, Dephasing time of GaAs electron-spin qubits coupled to a nuclear bath exceeding 200μs, Nat. Phys. **7**, 109 (2010).

[34] R. Stockill, C. Le Gall, C. Matthiesen, L. Huthmacher, E. Clarke, M. Hugues, and M. Atatüre, Quantum dot spin coherence governed by a strained nuclear environment, Nat. Commun. **7**, 12745 (2016).

[35] B. Eble, O. Krebs, A. Lemaître, K. Kowalik, A. Kudelski, P. Voisin, B. Urbaszek, X. Marie, and T. Amand, Dynamic nuclear polarization of a single charge-tunable InAs/GaAs quantum dot, Phys. Rev. B **74**, 081306 (2006).

[36] J. R. Petta, J. M. Taylor, A. C. Johnson, A. Yacoby, M. D. Lukin, C. M. Marcus, M. P. Hanson, and A. C. Gossard, Dynamic Nuclear Polarization with Single Electron Spins, Phys. Rev. Lett. **100**, 067601 (2008).

[37] G. Éthier-Majcher, D. Gangloff, R. Stockill, E. Clarke, M. Hugues, C. Le Gall, and M. Atatüre, Improving a Solid-State Qubit Through an Engineered Mesoscopic Environment, Phys. Rev. Lett. **119**, 130503 (2017).

[38] The small Rabi energies entail that any dephasing due to the optical ac-Stark shift is negligible, although in principle ac-Stark shift tuning could be employed to significantly reduce the dephasing due to charge noise [88].

[39] J. N. Becker, J. Görlitz, C. Arend, M. Markham, and C. Becher, Ultrafast all-optical coherent control of single silicon vacancy color centres in diamond, Nat. Commun. **7**, 13512 (2016).

[40] C. G. Yale, B. B. Buckley, D. J. Christle, G. Burkard, F. J. Heremans, L. C. Bassett, and D. D. Awschalom, All-optical control of a solid-state spin using coherent dark states, Proc. Natl. Acad. Sci. USA **110**, 7595 (2013).

[41] S. Novikov, T. Sweeney, J. E. Robinson, S. P. Premaratne, B. Suri, F. C. Wellstood, and B. S. Palmer, Raman coherence in a circuit quantum electrodynamics lambda system, Nat. Phys. **12**, 75 (2015).

[42] Q.-C. Liu, T.-F. Li, X.-Q. Luo, H. Zhao, W. Xiong, Y.-S. Zhang, Z. Chen, J. S. Liu, W. Chen, F. Nori, J. S. Tsai, and J. Q. You, Method for identifying electromagnetically induced transparency in a tunable circuit quantum electrodynamics system, Phys. Rev. A **93**, 053838 (2016).

[43] S. P. Premaratne, F. C. Wellstood, and B. S. Palmer, Characterization of coherent population-trapped states in a circuit-QED Λ system, Phys. Rev. A **96**, 043858 (2017).

[44] D. Loss and D. P. DiVincenzo, Quantum computation with quantum dots, Phys. Rev. A **57**, 120 (1998).

[45] J. Fischer, W. A. Coish, D. V. Bulaev, and D. Loss, Spin decoherence of a heavy hole coupled to nuclear spins in a quantum dot, Phys. Rev. B **78**, 155329 (2008).

[46] E. A. Chekhovich, A. B. Krysa, M. S. Skolnick, and A. I. Tartakovskii, Direct Measurement of the Hole-Nuclear Spin Interaction in Single InP/GaInP Quantum Dots Using Photoluminescence Spectroscopy, Phys. Rev. Lett. **106**, 027402 (2011).

[47] P. Fallahi, S. T. Yılmaz, and A. Imamoğlu, Measurement of a Heavy-Hole Hyperfine Interaction in InGaAs Quantum Dots Using Resonance Fluorescence, Phys. Rev. Lett. **105**, 257402 (2010).

[48] D. V. Bulaev and Daniel Loss, Spin Relaxation and Decoherence of Holes in Quantum Dots, Phys. Rev. Lett. **95**, 076805 (2005).

[49] K. De Greve, P. L. McMahon, D. Press, T. D. Ladd, D. Bisping, C. Schneider, M. Kamp, L. Worschech, S. Höfling, A. Forchel, and Y. Yamamoto, Ultrafast coherent control and suppressed nuclear feedback of a single quantum dot hole qubit, Nat. Phys. **7**, 872 (2011).

[50] C. Emary, X. Xu, D. G. Steel, S. Saikin, and L. J. Sham, Fast Initialization of the Spin State of an Electron in a Quantum Dot in the Voigt Configuration, Phys. Rev. Lett. **98**, 047401 (2007).

[51] G. Fernandez, T. Volz, R. Desbuquois, A. Badolato, and A. Imamoğlu, Optically Tunable Spontaneous Raman Fluorescence From a Single Self-Assembled InGaAs Quantum Dot, Phys. Rev. Lett. **103**, 087406 (2009).

[52] Z. Sun, A. Delteil, S. Faelt, and A. Imamoğlu, Measurement of spin coherence using Raman scattering, Phys. Rev. B **93**, 241302 (2016).

[53] A. Delteil, Z. Sun, Wei-bo Gao, E. Togan, S. Faelt, and A. Imamoğlu, Generation of heralded entanglement between distant hole spins, Nat. Phys. **12**, 218 (2015).

[54] R. Stockill, M. J. Stanley, L. Huthmacher, E. Clarke, M. Hugues, A. J. Miller, C. Matthiesen, C. Le Gall, and M. Atatüre, Phase-Tuned Entangled State Generation Between Distant Spin Qubits, Phys. Rev. Lett. **119**, 010503 (2017).

[55] J. R. Johansson, P. D. Nation, and F. Nori, QuTiP: An open-source Python framework for the dynamics of open quantum systems, Comput. Phys. Commun. **183**, 1760 (2012).

[56] J. R. Johansson, P. D. Nation, and F. Nori, QuTiP 2: A Python framework for the dynamics of open quantum systems, Comput. Phys. Commun. **184**, 1234 (2013).

[57] In practice, this assumption limits the size of the LCs that can be produced in this approach to less than 10.

[58] Time stamping these photons does not impose any experimental challenges, as detector setups with ≈30 ps readily resolve these phases due to the precession time being of the order of ∼2 ns for an external field of 100 mT.

[59] We assume η is the probability of obtaining a detector click if a photon was produced by the QD, i.e., it also includes any photon losses in the setup.

[60] The numerical calculations were performed using the Overhauser ensemble-averaged matrix operations defined in Appendix E.

[61] M. Popp, F. Verstraete, M. A. Martín-Delgado, and J. I. Cirac, Localizable entanglement, Phys. Rev. A **71**, 042306 (2005).

[62] S. Morley-Short, S. Bartolucci, M. Gimeno-Segovia, P. Shadbolt, H. Cable, and T. Rudolph, Physical-depth architectural requirements for generating universal photonic cluster states, Quantum Sci. Technol. **3**, 015005 (2018).

[63] J. H. Prechtel, A. V. Kuhlmann, J. Houel, A. Ludwig, S. R. Valentin, A. D. Wieck, and R. J. Warburton, Decoupling a hole spin qubit from the nuclear spins, Nat. Mater. **15**, 981 (2016).

[64] The anisotropy in the hole g factor is, in general, not the same as the effective anisotropy in the g tensor for the hole Overhauser shift due to hlh-lh mixing.

[65] The averages are performed independently due to the statistical independence of B_N^x and δT.

[66] J. Iles-Smith, D. P. S. McCutcheon, J. Mørk, and A. Nazir, Limits to coherent scattering and photon coalescence from solid-state quantum emitters, Phys. Rev. B **95**, 201305 (2017).

[67] Admixture of conduction band states even in the absence of a lh contribution may result in a non-Ising-type hyperfine Hamiltonian for the hh system [63], however, this goes beyond the scope of this work.

[68] M. Zieliński, Y. Don, and D. Gershoni, Atomistic theory of dark excitons in self-assembled quantum dots of reduced symmetry, Phys. Rev. B **91**, 085403 (2015).

[69] M. A. Dupertuis, K. F. Karlsson, D. Y. Oberli, E. Pelucchi, A. Rudra, P. O. Holtz, and E. Kapon, Symmetries and the Polarized Optical Spectra of Exciton Complexes in Quantum Dots, Phys. Rev. Lett. **107**, 127403 (2011).

[70] Y. Don, M. Zielinski, and D. Gershoni, The Optical Activity of the Dark Exciton, arXiv:1601.05530.

[71] D. Gross, K. Kieling, and J. Eisert, Potential and limits to cluster-state quantum computing using probabilistic gates, Phys. Rev. A **74**, 042343 (2006).

[72] M. Gimeno-Segovia, P. Shadbolt, D. E. Browne, and T. Rudolph, From Three-Photon Greenberger-Horne-Zeilinger States to Ballistic Universal Quantum Computation, Phys. Rev. Lett. **115**, 020502 (2015).

[73] E. A. Stinaff, M. Scheibner, A. S. Bracker, I. V. Ponomarev, V. L. Korenev, M. E. Ware, M. F. Doty, T. L. Reinecke, and D. Gammon, Optical signatures of coupled quantum dots, Science **311**, 636 (2006).

[74] H. J. Krenner, M. Sabathil, E. C. Clark, A. Kress, D. Schuh, M. Bichler, G. Abstreiter, and J. J. Finley, Direct Observation of Controlled Coupling in an Individual Quantum Dot Molecule, Phys. Rev. Lett. **94**, 057402 (2005).

[75] D. Kim, S. G. Carter, A. Greilich, A. S. Bracker, and D. Gammon, Ultrafast optical control of entanglement between two quantum-dot spins, Nat. Phys. **7**, 223 (2011).

[76] R. Songmuang, S. Kiravittaya, and O. G. Schmidt, Formation of lateral quantum dot molecules around self-assembled nanoholes, Appl. Phys. Lett. **82**, 2892 (2003).

[77] L. Wang, A. Rastelli, S. Kiravittaya, P. Atkinson, F. Ding, C. C. Bof Bufon, C. Hermannstaedter, M. Witzany, G. J. Beirne, P. Michler, and O. G. Schmidt, Towards deterministically controlled InGaAs/GaAs lateral quantum dot molecules, New J. Phys. **10**, 045010 (2008).

[78] P. M. Vora, A. S. Bracker, S. G. Carter, T. M. Sweeney, M. Kim, C. S. Kim, L. Yang, P. G. Brereton, S. E. Economou, and D. Gammon, Spin-cavity interactions between a quantum dot molecule and a photonic crystal cavity, Nat. Commun. **6**, 7665 (2015).

[79] N. Shaji, C. B. Simmons, M. Thalakulam, L. J. Klein, H. Qin, H. Luo, D. E. Savage, M. G. Lagally, A. J. Rimberg, R. Joynt, M. Friesen, R. H. Blick, S. N. Coppersmith, and M. A. Eriksson, Spin blockade and lifetime-enhanced transport in a few-electron si/sige double quantum dot, Nat. Phys. **4**, 540 (2008).

[80] A. Greilich, S. G. Carter, D. Kim, A. S. Bracker, and D. Gammon, Optical control of one and two hole spins in interacting quantum dots, Nat. Photonics **5**, 702 (2011).

[81] K. M. Weiss, J. M. Elzerman, Y. L. Delley, J. Miguel-Sanchez, and A. Imamoğlu, Coherent Two-Electron Spin Qubits in an Optically Active Pair of Coupled InGaAs Quantum Dots, Phys. Rev. Lett. **109**, 107401 (2012).

[82] J. M. Elzerman, K. M. Weiss, J. Miguel-Sanchez, and A. Imamoğlu, Optical Amplification Using Raman Transitions Between Spin-Singlet and Spin-Triplet States of a Pair of Coupled InGaAs Quantum Dots, Phys. Rev. Lett. **107**, 017401 (2011).

[83] A. N. Vamivakas, C.-Y. Lu, C. Matthiesen, Y. Zhao, S. Fält, A. Badolato, and M. Atatüre, Observation of spin-dependent quantum jumps via quantum dot resonance fluorescence, Nature (London) **467**, 297 (2010).

[84] D. Kim, S. E. Economou, Ş. C. Bădescu, M. Scheibner, A. S. Bracker, M. Bashkansky, T. L. Reinecke, and D. Gammon, Optical Spin Initialization and Nondestructive Measurement in a Quantum Dot Molecule, Phys. Rev. Lett. **101**, 236804 (2008).

[85] E. Bolduc, G. C. Knee, E. M. Gauger, and J. Leach, Projected gradient descent algorithms for quantum state tomography, npj Quantum Information **3**, 44 (2017).

[86] D. F. V. James, P. G. Kwiat, W. J. Munro, and A. G. White, Measurement of qubits, Phys. Rev. A **64**, 052312 (2001).

[87] M. Pari and J. Rehacek, *Quantum State Estimation*, Lecture Notes in Physics (Springer, Berlin, 2004).

[88] A. J. Ramsay, Passive stabilization of a hole spin qubit using the optical Stark effect, Phys. Rev. B **93**, 075303 (2016).